Arterial Waveguide Model for Shear Wave Elastography: Implementation and *In Vitro* Validation

Ali Vaziri Astaneh[1,5], Matthew W. Urban[2,4] Wilkins Aquino[3], James F. Greenleaf[2], Murthy N. Guddati[1*]

[1] *Department of Civil Engineering, North Carolina State University, Raleigh, NC 27695, USA*
[2] *Department of Physiology and Biomedical Engineering, Mayo Clinic, Rochester, MN, 55905, USA*
[3] *Department of Civil and Environmental Engineering, Duke University, Durham, NC, 27708, USA*
[4] *Department of Radiology, Mayo Clinic, Rochester, MN 55905, USA*
[5] *Institute for Computational Engineering and Sciences, University of Texas at Austin, Austin, TX 78712, USA*

Abstract

Arterial stiffness is found to be an early indicator of many cardiovascular diseases. Among various techniques, shear wave elastography has emerged as a promising tool to estimate local arterial stiffness from observed dispersion of guided waves. In this paper, we develop efficient models for computational simulation of guided wave dispersion in arterial walls. The models are capable of considering fluid-loaded tubes, immersed in fluid or embedded in solid, which are encountered for *in vitro/ex vivo*, and *in vivo* experiments. The proposed methods are based on judiciously combining Fourier transformation and finite element discretization, leading to significant reduction in computational cost while fully capturing the complex three-dimensional wave propagation. The developed methods are implemented in open-source code, and verified by comparing with significantly more expensive, fully three-dimensional finite element models. We also validate the models using shear wave elastography of tissue-mimicking phantoms. The computational efficiency of the developed methods indicates the possibility of leading to real-time estimation of arterial stiffness, which would be beneficial in clinical settings.

Keywords: arterial stiffness, guided waves, finite element, viscoelasticity, fluid-structure interaction

1. Introduction

It has been established that variation of arterial mechanical properties are correlated to various cardiovascular diseases [1-5]. For instance, increased arterial stiffness is associated with high risk of stroke [4, 6-8], myocardial infarction [9], end stage renal disease [10], diabetes [11], hypertension [12-15], and atherosclerosis development [8, 16]. Decreases in arterial stiffness can also occur in some cases, such as aneurysm [17]. Therefore, improving the prognostic ability and diagnosis techniques for early detection of arterial variations, has been attracting a widespread attention to decrease cardiovascular mortality rates.

Several methods have been introduced to measure the arterial stiffness globally and locally. One of the most common global techniques is based on analysis of arterial pulse wave traveling through the artery which can provide an estimate of the Young's modulus of the arterial wall [18-20]. Despite its widespread acceptance, it suffers from several limitations; distance measurement is prone to error [21]; time measurement requires consideration of a relatively long distance due to low resolution [22], boundary

* Corresponding author. Tel.: +1 919 515 7699; fax: +1 919 515 7908
E-mail address: murthy.guddati@ncsu.edu

conditions are unrealistic (isolation in vacuum and carrying inviscid fluid [23]), and finally linearization of Euler fluid dynamic equation [24] despite strongly nonlinear propagation of the pulse wave. Therefore, measuring the Pulse Wave Velocity (PWV) only provides an average modulus of the arterial tree throughout the length measured, most typically involving the aorta.

As arterial properties vary at different sites [17, 25], a local, instantaneous and quantitative modulus estimator is highly desirable. In recent years, Acoustic Radiation Force (ARF)-based imaging has formed a well-known noninvasive tool for localized tissue characterization. In ARF-based methods, an ultrasonic wave is transmitted into the tissue and the motion is monitored spatially and temporally using phase shift or cross-correlation based algorithms. In general, ARF methods can be categorized based on the type of excitation pulses as (a) quasi-static: such as sonorheometry [26]; (b) transient: such as acoustic radiation force impulse imaging [27], shear wave elasticity imaging [28], supersonic shear imaging [29], shear wave spectroscopy [30], and spatially modulated ultrasound radiation force [31]; and (c) harmonic: such as vibro-acoustography [32], harmonic motion imaging [33], crawling wave spectroscopy [34], and shearwave dispersion ultrasound vibrometery [35, 36]. The description of the various ARF methods can be found in [37].

Among the imaging techniques, shear wave elastography (SWE) has emerged as a promising diagnostic tool in the estimation of shear wave speed, which is directly correlated to the tissue mechanical properties. To date, SWE has been examined for various organs such as liver [36], kidney [38], prostate [39], bladder wall [40] and arterial wall [22, 41]. In bulk tissues, boundary conditions do not significantly affect shear waves propagation. However, in confined geometries such as thin layered organs, shear waves become guided and dispersive, i.e. they travel with different velocities at different frequencies. This phenomena makes the property assessment more complicated, but on the other hand sensitivity of different wave modes provides additional information that can be used for detecting possible anisotropic architecture [42] or fiber orientation [43].

Strong contrast between the arterial wall shear wave velocity and the external tissue (and internal blood) facilitates guided propagation of shear waves in arterial walls. For mathematical modeling and to reduce the complexity of the analytical solutions for cylindrical waves [44, 45], an immersed plate has been examined in many studies as an approximate model [22, 23, 46-51]. Another approximation is wave propagation in annuli (see e.g. [52]). More complicated practiced models include the hollow tube [41, 53], fluid-filled tube [53, 54], and the recent immersed and fluid-filled 3D finite element model [55]. Also similar researches have been conducted for studying the guided wave propagation in bones [56-59].

In this work, in a simultaneous effort to improve the accuracy and efficiency of mathematical modeling, we propose an extremely efficient model based on cylindrical waveguide formulation that allows consideration of fluid inside as well as fluid or tissue around the tube. The exterior fluid simulates the *in vitro*/*ex vivo* experimental setups and the exterior tissue is suitable for *in vivo* tests. We provide a brief but inclusive formulation, open-source implementation [60], verification, and *in vitro* validation of the presented approach using vessel-mimicking phantoms.

2. Shear wave elastography

As arteries are hollow cylindrical structures filled with liquid (blood) and embedded in a softer surrounding tissue, shear waves become guided and undergo dispersion that is affected by the geometry and modulus of the artery. The geometry and modulus can thus be estimated by examining the dispersion properties of guided waves, which is the basis for SWE. As shown in Figure 1, SWE involves three steps. (i) Acquisition of data is performed by applying an ultrasonic pulse excitation focused on the wall of the

artery to generate shear waves propagating along the arterial wall (Figure 1 (a)). Propagation is then measured by recording the normal particle displacement at the top of the wall or averaged through the wall; an example displacement measurement, obtained from a phantom tube, is shown in Figure 1 (b). (ii) The displacement is transformed in space and time to obtain frequency-wavenumber (f-k) representation as shown in Figure 1 (c) (see [22]). The peaks in the f-k displacement can be processed to obtain phase velocities $(c_p = f / k)$ of different wave modes as a function of frequency (see Figure 1 (d)); and (iii) the final step is to estimate the arterial modulus by inversion, i.e. back-calculate the modulus by matching the measured dispersion curves in Figure 1 (d).

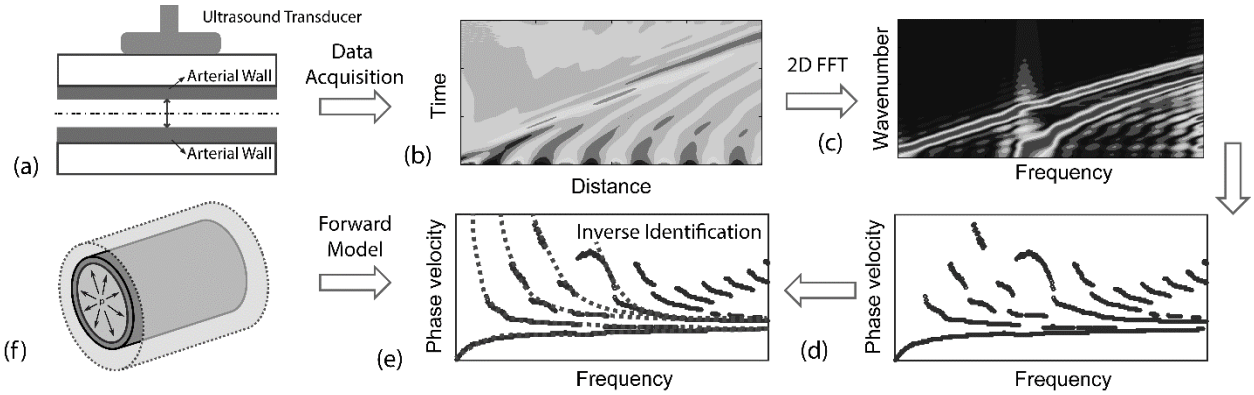

Figure 1 Schematic of the steps in SWE to determine arterial material properties: (a) experimental setup where the guided waves are generated and recorded at the surface; (b) trace representing the measured response histories; (c) transformed signal in frequency-wavenumber (f-k) domain; (d) dispersion curves obtained by processing the f-k signal; (e) properties estimated through inversion, i.e. matching the measured dispersion curves with those computed from (f) the forward model.

Inversion of the dispersion data, i.e. back-calculating arterial properties from measured dispersion data in Figure 1 (d), is performed through an optimization procedure, where the difference in measured and simulated dispersion curves is minimized. The simulated dispersion curves are obtained with the help of so-called forward model, which takes as input the geometry and modulus of the artery, and computes the theoretical dispersion curves. Since the iterative inversion procedure often requires a large number of forward models, efficiency of forward models is a critical first step and forms the focus of the present contribution. Specifically, we develop robust three-dimensional models based on efficient semi-analytical waveguide formulation, which are discussed in the remainder of the paper.

3. Semi-analytical finite element (SAFE) method for waveguides

In this paper we introduce semi-analytical models for forward modeling of the immersed and fluid-filled tubes with cylindrical and non-cylindrical cross-sections. The proposed approach, while capturing full three-dimensional tube motion, significantly reduces the computational cost as it only requires a one-dimensional (1D) discretization for cylindrical cross-sections and two-dimensional (2D) discretization for non-cylindrical cross-sections. The resulting efficiency increase is expected to eventually facilitate fast SWE inversion. In this section, starting with general governing differential equations, we derive a model requiring only 2D discretization for cylindrical and noncylindrical waveguides. In the subsequent section, we derive an even more efficient model requiring only radial discretization, when the waveguide is cylindrical. We have provided the implementation of these methods in an open-source MATLAB® software named WaveDisp [60].

3.1 Governing equations

Consider the waveguide in Figure 2 (a), where a solid tube is filled with fluid and immersed in infinite fluid. The governing equations include the elastodynamic equation for the solid tube, acoustic wave equations for the fluid, interface conditions for the solid-fluid interface, and the radiation condition for the fluid at infinity, namely,

$$-\mathbf{L}_\sigma^T\boldsymbol{\sigma}+\rho_S\ddot{\mathbf{U}}=\mathbf{0}, \qquad \text{in} \quad \Omega_S, \tag{1a}$$

$$-\nabla_{\mathbf{x}}\cdot\left(\frac{1}{\rho_F}\nabla_{\mathbf{x}}P\right)+\frac{1}{\rho_F c_F^2}\ddot{P}=0, \qquad \text{in} \quad \Omega_F, \tag{1b}$$

$$\bar{\boldsymbol{\sigma}}\cdot\mathbf{n}_S-P\mathbf{n}_F=\mathbf{0}, \qquad \text{on} \quad \Gamma_{FS}, \tag{1c}$$

$$\rho_F\ddot{\mathbf{U}}\cdot\mathbf{n}_S-\frac{\partial P}{\partial \mathbf{n}_F}=0, \qquad \text{on} \quad \Gamma_{FS}, \tag{1c}$$

$$r\left(\frac{\partial P}{\partial r}+\frac{1}{c_F}\dot{P}\right)=0, \qquad \text{as} \quad r\to\infty, \tag{1d}$$

where $\mathbf{U}$ and $\boldsymbol{\sigma}$ are the displacement and stress vectors in the solid domain Ω_S, P is the pressure field in the fluid domain Ω_F, ρ_S is the solid medium density, and ρ_F and c_F are the density and pressure wave velocity of the fluid medium, respectively. Note that $\mathbf{L}_\sigma(\cdot)$ is the symmetric gradient matrix operator, and $\nabla_{\mathbf{x}}\cdot(\cdot)$ and $\nabla_{\mathbf{x}}(\cdot)$ are divergence and gradient defined in the system of coordinates $\mathbf{x}=(x_1,x_2,x_3)$. The solid-fluid interface is represented by Γ_{FS}, $\bar{\boldsymbol{\sigma}}$ is the tensor representation of the stress vector $\boldsymbol{\sigma}$, r denotes the radius, and $\mathbf{n}_S$ and $\mathbf{n}_F$ are respectively the unit vectors for the solid and fluid domains.

Remark on nonlinearity: The use of *linear* elastodynamic and acoustic equations are justified given that the ARF excitation causes small deformations and stresses in the artery, and small changes in the acoustic pressure in the blood and surrounding fluid. Moreover, the ARF excitation and the associated data acquisition is performed in a very short period compared to the cardiac cycle. This indicates that there is no significant change in the blood pressure and the resulting hoop stresses. Thus, while the arterial modulus is governed by the prestress of the artery itself and may change within the cardiac cycle, our eventual goal is to estimate the *tangent* modulus at the instance of ARF excitation and data acquisition.

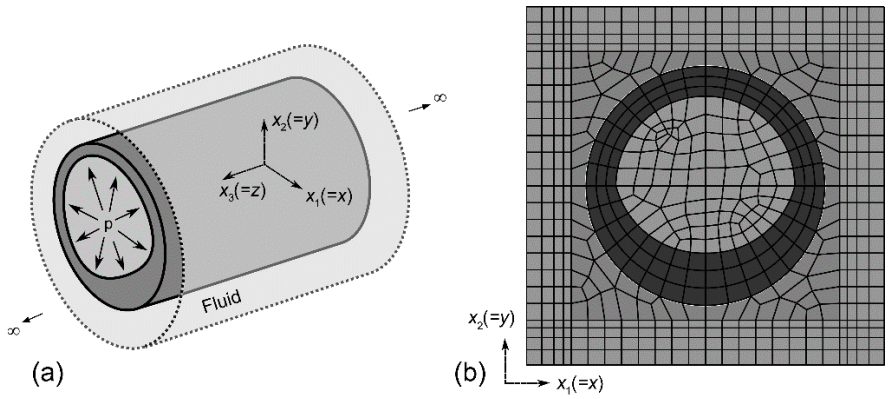

Figure 2 (a) Geometry of the three-dimensional (3D) waveguide, and (b) 2D discretization of solid cross-section fluid buffer region and infinite fluid with perfectly matched discrete layer (PMDL) elements.

3.2 Dispersion relation: continuous eigenvalue problem

Given that the objective is to obtain the dispersion relations, i.e. axial wavenumber – frequency pairs that satisfy the governing equation, we consider displacements and pressures of the form, $\mathbf{U} = \mathbf{u}(x_1, x_2)e^{-i\omega t + ik_z z}$ and $P = p(x_1, x_2)e^{-i\omega t + ik_z z}$, where $\omega \in \mathbb{R}$ is the temporal frequency and $k_z \in \mathbb{C}$ is the longitudinal wavenumber. This leads to a continuous eigenvalue problem of finding the (ω, k_z) pairs that satisfy the following equations with the eigenvector $\{\mathbf{u}^T \; p\}^T$:

$$k_z^2\left(\mathbf{D}_{zz}\mathbf{u}\right) - ik_z\left(\mathbf{D}_{z\mathfrak{x}}\mathbf{L}_{z\mathfrak{x}}\mathbf{u}\right) - \mathbf{L}_{z\mathfrak{x}}\left(\mathbf{D}_{\mathfrak{x}z}ik_z\mathbf{u}\right) - \mathbf{L}^1_{\mathfrak{x}\mathfrak{x}}\left(\mathbf{D}_{\mathfrak{x}\mathfrak{x}}\mathbf{L}^2_{\mathfrak{x}\mathfrak{x}}\mathbf{u}\right) - \rho_S\omega^2\mathbf{u} = \mathbf{0}, \quad \text{in} \quad \Omega_S, \tag{2a}$$

$$\frac{k_z^2}{\rho_F}p - \nabla_{\mathfrak{x}}\cdot\left(\frac{1}{\rho_F}\nabla_{\mathfrak{x}}\, p\right) - \frac{\omega^2}{\rho_F c_F^2}p = 0, \quad \text{in} \quad \Omega_F, \tag{2b}$$

$$\bar{\boldsymbol{\sigma}}\mathbf{n}_S - p\mathbf{n}_F = 0, \quad \text{and} \quad -\omega^2\rho_F\mathbf{u}\cdot\mathbf{n}_S - \frac{\partial p}{\partial \mathbf{n}_F} = 0, \quad \text{on} \quad \Gamma_{FS}, \tag{2c}$$

$$r\left(\frac{\partial p}{\partial r} - \frac{i\omega}{c_F}p\right) = 0, \quad \text{as} \quad r \to \infty, \tag{2d}$$

where $\mathfrak{X} = (x_1, x_2)$ represents the system of coordinates in the cross-section. Note that $\mathbf{D}_{zz}$, $\mathbf{D}_{z\mathfrak{x}}$, $\mathbf{D}_{\mathfrak{x}z}$, $\mathbf{D}_{\mathfrak{x}\mathfrak{x}}$ are the material property coefficients and $\mathbf{L}_{z\mathfrak{x}}$, $\mathbf{L}_{z\mathfrak{x}}$, $\mathbf{L}^1_{\mathfrak{x}\mathfrak{x}}$, $\mathbf{L}^2_{\mathfrak{x}\mathfrak{x}}$ are the matrix operators, which can be derived from $\mathbf{L}_\sigma(\cdot)$ in (1a), for different system of coordinates. The above continuous eigenvalue problem forms the basis for waveguide dispersion analysis.

3.3 Semi-analytical finite element method (SAFE) for noncircular cross-sections

To discretize the eigenvalue problem in (2), the domain is discretized through finite element approximation within the cross-section, which is often referred to as semi-analytical finite element (SAFE) method [45] (also referred to as thin-layer method in the contexts of geophysics [61]). The reason for the name is that analytical expansion is needed in the z direction (of the form $\mathbf{U} = \mathbf{u}(x_1, x_2)e^{-i\omega t + ik_z z}$), while finite element discretization is employed across the cross-section, e.g. the waveguide shown in Figure 2 (a) is discretized with a two-dimensional mesh as shown in Figure 2 (b). Note that distortion in the mesh deteriorates the numerical convergence, thus care must be exercised while using unstructured grids. Alternatively, a mapped mesh can be used whenever possible.

We elaborate this approach by starting with more details of the governing equation, where Cartesian coordinates are used in the cross-section. Thus, in the solid domain, elastodynamic equation for the harmonic waves is given in Equations (2a) and (1a). In this problem, $\mathbf{u} = \{u_x \; u_y \; u_z\}^T$ is the displacement vector and the stress vector $\boldsymbol{\sigma} = \mathbf{D}\boldsymbol{\varepsilon} = \{\sigma_{xx} \; \sigma_{yy} \; \sigma_{zz} \; \sigma_{yz} \; \sigma_{xz} \; \sigma_{xy}\}^T$ is related to the strain vector $\boldsymbol{\varepsilon} = \mathbf{L}_\varepsilon\mathbf{u} = \{\varepsilon_{xx} \; \varepsilon_{yy} \; \varepsilon_{zz} \; \gamma_{yz} \; \gamma_{xz} \; \gamma_{xy}\}^T$ through $\mathbf{D}_{6\times 6}$ where the nonzero entries for an isotropic medium are $D_{11} = D_{22} = D_{33} = \rho_S c_p^2$, $D_{44} = D_{55} = D_{66} = \rho_S c_s^2$ and $D_{12} = D_{21} = D_{13} = D_{31} = D_{23} = D_{32} = \rho_S(c_p^2 - 2c_s^2)$. Parameters $c_s = (G/\rho_S)^{1/2}$ and $c_p = c_s\left((2-2\nu)/(1-2\nu)\right)^{1/2}$ are the shear and pressure wave velocity

where G, ν are the solid medium shear modulus and Poisson's ratio, respectively. The nonzero entries of 6×3 matrix operators $\mathbf{L}_\sigma$ and $\mathbf{L}_\varepsilon$ are,

$$\begin{aligned}\mathbf{L}_\sigma(\cdot)=\mathbf{L}_\varepsilon(\cdot)=\mathbf{L}_x\frac{\partial}{\partial x}+\mathbf{L}_y\frac{\partial}{\partial y}+\mathbf{L}_z\, ik_z,\ \text{with}\ \ \mathbf{L}_x^S(1,1)=\mathbf{L}_x^S(5,3)=\mathbf{L}_x^S(6,2)=1,\\ \mathbf{L}_y^S(2,2)=\mathbf{L}_y^S(4,3)=\mathbf{L}_y^S(6,1)=1,\quad \text{and}\quad \mathbf{L}_z^S(3,3)=\mathbf{L}_z^S(4,2)=\mathbf{L}_z^S(5,1)=1.\end{aligned} \tag{3}$$

In the fluid domain, the equation of motion in (2b) with constant ρ_F takes the form,

$$-\frac{1}{\rho_F}\nabla^2 p+\frac{1}{\rho_F}\left(k_z^2-\frac{\omega^2}{c_F^2}\right)p=0, \tag{4}$$

where $\nabla^2(\cdot)=\partial^2(\cdot)/\partial x^2+\partial^2(\cdot)/\partial y^2$.

The main idea of the SAFE method is to discretize the field variables $\mathbf{u}$ and p in the cross-section, i.e. $\mathbf{u}(x,y)=\mathbf{N}_S(x,y)\bar{\mathbf{u}}$ and $p(x,y)=\mathbf{N}_F(x,y)\bar{p}$, where $\mathbf{N}_S, \mathbf{N}_F$ are the finite element shape functions for solid and fluid domains, respectively. Substituting these in continuous eigenvalue problem in Equations (2) results in the discrete version:

$$\left(k_z^2\begin{bmatrix}\mathbf{K}_2^S & \mathbf{0}\\ \mathbf{0} & \kappa\mathbf{K}_2^F\end{bmatrix}+\begin{bmatrix}\mathbf{K}_0^S-\omega^2\mathbf{M}^S & -\kappa\mathbf{C}_{SF}\\ -\omega^2\mathbf{C}_{SF}^T & \kappa(\mathbf{K}_0^F-\omega^2\mathbf{M}^F)\end{bmatrix}\right)\begin{Bmatrix}\boldsymbol{\phi}_S\\ \boldsymbol{\phi}_F\end{Bmatrix}=\begin{Bmatrix}\mathbf{0}\\ \mathbf{0}\end{Bmatrix}, \tag{5}$$

where $\kappa=\|\mathbf{K}_2^S\|_{\text{inf}}/\|\mathbf{K}_2^F\|_{\text{inf}}$ is the normalization factor that improves the conditioning of the system. Contribution matrices of solid domain $\mathbf{K}_2^S, \mathbf{K}_0^S, \mathbf{M}^S$, fluid medium $\mathbf{K}_2^F, \mathbf{K}_0^F, \mathbf{M}^F$ and the fluid-structure interaction matrix $\mathbf{C}_{SF}$ are defined in Appendix A.

Clearly the accuracy of the dispersion relation from the discrete eigenvalue problem in Equation (5) is determined by the discretization of the field variables in the cross-section. As shown in Figure 2 (b), the solid domain, and the fluid inside, if any, are discretized in 2D with high-order FEM. Also, a rectangular fluid region surrounding the fluid is discretized with finite elements. The discretization of the fluid-structure interface condition in Equation (2c) is performed in a consistent way, as described in Section 5.5.1 of [62]. Fluid outside the tube is discretized using perfectly matched discrete layers (PMDL) [63, 64], which is a discrete variant of the highly successful perfectly matched layers (PML) [65]. The details of the PMDL discretization can also be found in Section 5.5.2 of [62].

3.4 Filtering of dispersion curves

The discrete eigenvalue problem in Equation (5) is solved by sweeping through frequency, resulting in (ω, k_z) pairs, where $\mathrm{i}=1,..,n_{\text{mode}}$ represents the index of propagation modes. These dispersion curves are often presented as phase velocities $c_{\text{ph}}^{\mathrm{i}}=\omega/\Re(k_z^{\mathrm{i}})$, plotted as a function of frequency. Attenuation curves are plotted as the imaginary part of the wavenumbers, i.e. $\alpha^{\mathrm{i}}=\Im(k_z^{\mathrm{i}})$. It must however be noted that not all the eigenvalue pairs are necessarily observed in experimental data. Picking out the feasible solutions depends on the physics of the problem. For the soft materials considered in this paper, as discussed above, energy inside the solid domain does not leak into the fluid domain. Therefore to obtain

these non-leaky waves, one should only choose the purely real wavenumbers k_z and ignore the complex k_z solutions. Besides, the phase velocity of the non-leaky wave modes cannot exceed the pressure wave velocity in the fluid, therefore the criterion $\omega / k_z < \min(c_f, c_{\text{ph}}^{\max})$ has to be considered as well, where $c_{\text{ph}}^{\max}$ is the maximum desired phase velocity.

3.5 Group velocity computation

By writing (5) in the form $\mathbf{K}\boldsymbol{\phi}_{\text{R}} = \mathbf{0}$, or $\boldsymbol{\phi}_{\text{L}}^{\dagger}\mathbf{K} = \mathbf{0}$ where $\mathbf{K}(\omega, k_z) = k_z^2\bar{\mathbf{A}} + \bar{\mathbf{C}}$ and $\boldsymbol{\phi}_{\text{R}}, \boldsymbol{\phi}_{\text{L}}$ are the right and left eigenvectors, group velocity can be obtained as,

$$c_g = -\Re\left(\frac{\boldsymbol{\phi}_{\text{L}}^{\dagger}(\partial\mathbf{K}/\partial k_z)\boldsymbol{\phi}_{\text{R}}}{\boldsymbol{\phi}_{\text{L}}^{\dagger}(\partial\mathbf{K}/\partial\omega)\boldsymbol{\phi}_{\text{R}}}\right). \tag{6}$$

Note that $\bar{\mathbf{A}}$ and $\bar{\mathbf{C}}$ can both be functions of frequency, e.g. in the contexts of viscoelasticity and frequency-dependent absorbing layers. It is worth mentioning that eigenvalue derivatives can be also obtained without computing the eigenvectors using the perturbation approach presented in Equation (10) of [66].

4. Fourier-Spectral SAFE method for axisymmetic waveguides

Given that arteries can plausibly be represented as axially symmetric (cylindrical) waveguides, we propose to exploit the geometry to further reduce the computational cost of SAFE method described in the previous section. Note that the proposed approach is motivated not by characterizing arteries with significant localized plaque, but early increase in arterial stiffness that is hypothesized to precede significant plaque formation [67, 68].

We employ Fourier series expansion in the azimuthal direction, and spectral finite elements in the radial direction. The advantage of the Fourier series is that the two-dimensional eigenvalue problem is decoupled into a set of one-dimensional eigenvalue problems in the radial direction. Use of spectral FEM in the radial direction further increases the efficiency of the problem, owing to the exponential convergence of spectral FEM. The remainder of the section contains the details of the formulation of the Fourier-Spectral SAFE method.

4.1 Dispersion relation for cylindrical waveguides

We use cylindrical coordinates for describing the waveguide geometry with axisymmetric cross sections as shown in Figure 3 (a). The elastodynamic equation of the solid tube for the harmonic waves (of the form $\mathbf{U} = \mathbf{u}(r,\theta)e^{-i\omega t + ik_z z}$) is given in Equations (2a) and (1a) , where here $\mathbf{u} = \{u_r \;\; u_\theta \;\; u_z\}^T$. The stress vector $\boldsymbol{\sigma} = \mathbf{D}\boldsymbol{\varepsilon} = \{\sigma_{rr} \;\; \sigma_{\theta\theta} \;\; \sigma_{zz} \;\; \sigma_{\theta z} \;\; \sigma_{rz} \;\; \sigma_{r\theta}\}^T$ is related to the strain vector $\boldsymbol{\varepsilon} = \mathbf{L}_\varepsilon\mathbf{u} = \{\varepsilon_{rr} \;\; \varepsilon_{\theta\theta} \;\; \varepsilon_{zz} \;\; \gamma_{\theta z} \;\; \gamma_{rz} \;\; \gamma_{r\theta}\}^T$ through $\mathbf{D}_{6\times6}$. The matrix operators $\mathbf{L}_\sigma$ and $\mathbf{L}_\varepsilon$ are as follows,

$$\begin{aligned}
\mathbf{L}_\sigma(\cdot) &= \mathbf{L}_r^S\frac{1}{r}\frac{\partial(\cdot\times r)}{\partial r} + \mathbf{L}_\theta^S\frac{1}{r}\frac{\partial(\cdot)}{\partial\theta} + \mathbf{L}_z^S ik_z - \mathbf{L}_o^S\frac{1}{r},\\
\mathbf{L}_\varepsilon(\cdot) &= \mathbf{L}_r^S\frac{\partial(\cdot)}{\partial r} + \mathbf{L}_\theta^S\frac{1}{r}\frac{\partial(\cdot)}{\partial\theta} + \mathbf{L}_z^S ik_z + \mathbf{L}_o^S\frac{1}{r},
\end{aligned} \tag{7}$$

where nonzero entries of 6×3 matrices $\mathbf{L}_r^S, \mathbf{L}_\theta^S, \mathbf{L}_z^S, \mathbf{L}_o^S$ are,

$$\begin{aligned}&\mathbf{L}_r^S(1,1)=\mathbf{L}_r^S(5,3)=\mathbf{L}_r^S(6,2)=1, \text{ and } \mathbf{L}_\theta^S(2,2)=\mathbf{L}_\theta^S(4,3)=\mathbf{L}_\theta^S(6,1)=1,\\ &\mathbf{L}_z^S(3,3)=\mathbf{L}_z^S(4,2)=\mathbf{L}_z^S(5,1)=1, \text{ and } \mathbf{L}_o^S(2,1)=-\mathbf{L}_o^S(6,2)=1.\end{aligned} \tag{8}$$

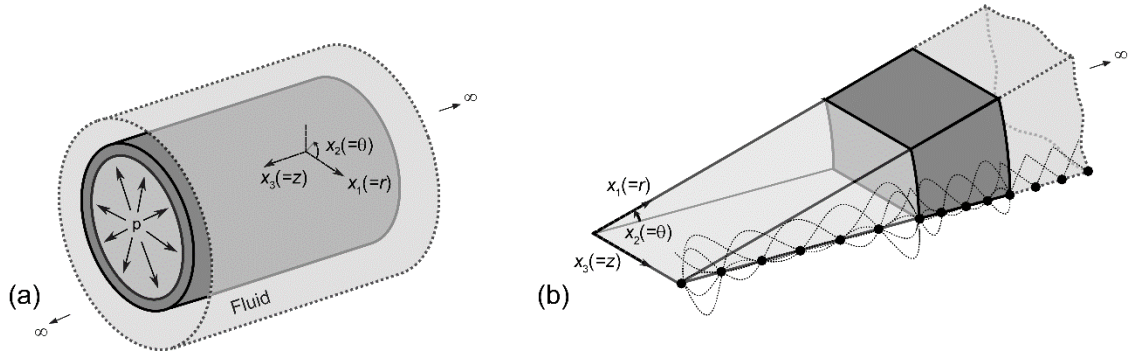

Figure 3 (a) Geometry of the immersed fluid-filled tube in 3D, and (b) 1D discretization of solid and inner fluid with high-order finite elements and linear PMDL elements for the exterior infinite fluid.

The acoustic equation in the fluid domain with constant ρ_F is given in (4) where $\nabla^2(\cdot)=r^{-1}\partial(r\times\partial(\cdot)/\partial r)/\partial r+r^{-2}\partial^2(\cdot)/\partial\theta^2$. The radiation condition for the fluid domain at infinity is given by (2c) and the interaction of fluid and structure at the interface are governed by the continuity of traction and balance of mass, given in (2d).

4.2 *Fourier series expansion in azimuthal direction*

The continuous eigenvalue problem in (2) using the operators defined in the previous section needs to be discretized in the r and θ directions. However, given the regularity of the cross-section, we employ more efficient Fourier-spectral discretization in place of discretizing the cross-section with finite elements. Specifically, after using Fourier transform in the longitudinal direction, we use Fourier series expansion in the azimuthal direction, namely $\mathbf{U}(r,\theta,z,t)=\mathbf{u}(r,n,k_z,\omega)e^{-i\omega t+ik_z z+in\theta}$ and $P(r,\theta,z,t)=p(r,n,k_z,\omega)e^{-i\omega t+ik_z z+in\theta}$ where $n=0,1,2,3,...$ is the circumferential Fourier number. This results in the decoupled system of 1D differential eigenvalue problems in the radial direction,

$$\begin{aligned}&\frac{-1}{r}\frac{\partial}{\partial r}\left(r\mathbf{D}_{rr}\partial\mathbf{u}/\partial r+in\mathbf{D}_{r\theta}\mathbf{u}+ik_z r\mathbf{D}_{rz}\mathbf{u}+\mathbf{D}_{ro}\mathbf{u}\right)+\frac{1}{r}\left(\mathbf{D}_{ro}^T-in\mathbf{D}_{r\theta}^T-ik_z\mathbf{D}_{rz}^T\right)\frac{\partial\mathbf{u}}{\partial r}\\ &\left(nk_z\mathbf{D}_{\theta z}-ik_z\mathbf{D}_{zo}+nk_z\mathbf{D}_{\theta z}^T+ik_z\mathbf{D}_{zo}^T+\mathbf{D}_{oo}\right)\frac{\mathbf{u}}{r}+\left(n^2\mathbf{D}_{\theta\theta}-in\mathbf{D}_{\theta o}+\mathbf{D}_{\theta o}^T in\right)\frac{\mathbf{u}}{r^2} \qquad \text{in } \Omega_S,\\ &\qquad +\left(k_z^2\mathbf{D}_{zz}\mathbf{u}-\rho_S\omega^2\mathbf{I}_{3\times 3}\right)\mathbf{u}=\mathbf{0},\\ &\frac{-1}{\rho_F r}\frac{\partial}{\partial r}\left(r\frac{\partial p}{\partial r}\right)+\left(k_z^2 p+\frac{n^2}{r^2}-\frac{\omega^2}{\rho_F c_F^2}\right)p=0, \qquad \text{in } \Omega_F,\end{aligned} \tag{9}$$

where $\mathbf{D}_{pq}=(\mathbf{L}_p^S)^T\mathbf{D}_{6\times 6}\mathbf{L}_q^S$ for $p,q\in\{r,\theta,z,o\}$ and $\mathbf{L}^S$ matrices are defined in (8). By discretizing the solution in the radial direction, i.e. $\mathbf{U}(r,\theta,z,t)=\mathbf{N}_S(r)\mathbf{u}(n,k_z,\omega)e^{-i\omega t+ik_z z+in\theta}$ and $P(r,\theta,z,t)=\mathbf{N}_F(r)p(n,k_z,\omega)e^{-i\omega t+ik_z z+in\theta}$ where $\mathbf{N}_S$, $\mathbf{N}_F$ are the solid and fluid domain shape functions

along the radius, the final discrete eigenvalue problem can be obtained as the one presented in (5) where $\mathbf{K}_2^S, \mathbf{K}_0^S, \mathbf{M}^S$, $\mathbf{K}_2^F, \mathbf{K}_0^F, \mathbf{M}^F$ and $\mathbf{C}_{SF}$ are presented in Appendix B. Note that these matrices are functions of circumferential Fourier number associated with different propagating modes. Note that any anisotropy can be simply included by using the desired 3D anisotropic coefficient matrix $\mathbf{D}_{6\times6}$, however it is not the focus of the current study.

4.2 Radial discretization: spectral FEM and PMDL

The formulation in (9) is valid irrespective of the numerical discretization employed in the radial direction. As shown in Figure 3 (b), the inner fluid and the tube are discretized with spectral finite elements for computational efficiency (due to exponential convergence).

For modeling the infinite fluid around the tube, Perfectly Matched Discrete Layers (PMDL) are used. Note that PMDL lengths must be chosen based on the underlying physics. When the shear wave velocity in the solid (e.g. tissue) is less than the acoustic wave velocity in the fluid, solid-born wavemodes are non-leaky or trapped (purely evanescent perpendicular to interface, see e.g. [69]). In order to model these modes properly, PMDL elements with purely real length should be used, which are best to choose as,

$$L_j = \frac{L_1 \alpha^{j-1}}{(n_{\mathrm{P}} + 1 - j)} \quad \text{with} \quad L_1 = \frac{2 c_f \omega_{\max}}{\sqrt{(c_f / c_{\mathrm{Sch}})^2 - 1}}, \quad j = 1, \ldots, n_{\mathrm{P}}. \tag{10}$$

where L_1 is the minimum length, α is the geometric (increase) ratio, $\omega_{\max}$ is the maximum frequency of interest for obtaining the dispersion curves, and c_{Sch} is the Scholte (interface) wave velocity, which can be computed from the closed-from expressions (see e.g. [70]). Note that often a handful of PMDL layers are sufficient to discretize the entire unbounded domain. Further details on the provided criterion in (10) can be found in Section 5.4.2 of [62].

Note that as *in vitro* experiments are done with phantoms or arteries immersed in fluid, PMDLs are used for modeling the infinite fluid around the tube. Also, because the proposed tube model can be multilayered [62], the surrounding fluid can be replaced by an additional solid (tissue) layer for *in vivo* experiments. However, considering an infinite tissue around the artery requires designing the PMDL layers to appropriately model the wave-propagation physics at the solid-solid interface, which is beyond the scope of this paper. Also note that the Fourier-Spectral SAFE formulation can employ other constitutive laws, e.g. including hyper elasticity and anisotropy (see reviews of existing models in [71-75]).

Remark on computational cost: For the example presented in the next (verification) section, the Fourier-Spectral SAFE model needs 1.98 seconds on a 2.83 GHz desktop computer, for 65 frequencies. The 3D FE model was run in parallel, and took 361 seconds on forty eight 3.1 GHz processors. Assuming 80% parallel efficiency, the Fourier-Spectral SAFE method is *7,700 times* more efficient than 3D FE model, while fully capturing the complicated 3D wave propagation and dispersion. Note further that the cost of Fourier-Spectral SAFE model can be further reduced by limiting the number of frequencies, further code optimization as well as utilizing modern computing platforms, e.g. graphical processing units (GPUs). Such techniques coupled with the already modest computational cost could eventually lead to real-time prediction of arterial stiffness using SWE data.

5. Verification

We verify the proposed models by comparing with fully three-dimensional finite element (FE) models previously employed for arteries [55]. To this end, we consider a rubber tube filled with and immersed in water. Inner radius of tube and the wall thickness are $r_{\text{in}} = 3\text{mm}$ and $h = 1\text{mm}$, respectively. Material properties of rubber are $G = 157\,\text{kPa}$, $\nu = 0.495$ and ρ_S=1037 kg/m^3. Bulk modulus of water is assumed to be $\kappa_F = 2.2\times10^9$ kPa with the density of ρ_F=1000 kg/m^3.

In the Fourier-Spectral SAFE model, the tube wall is discretized with one quartic (5-noded) finite element, and the inner fluid region is discretized using two quartic elements. To model the non-leaky waves we use 6 PMDL elements (with $\alpha = 4$ and $c_{\text{Sch}} = 10.36$ m/s using (10)). Figure 4 shows the calculated phase and group velocity curves for the circumferential Fourier number $n = 1$. The Figure also compares the curves with the first flexural mode of an immersed plate with the same thickness and material properties. It can be seen that the difference is significant, implying that use of plate models for inversion would lead to significant errors in modulus estimates.

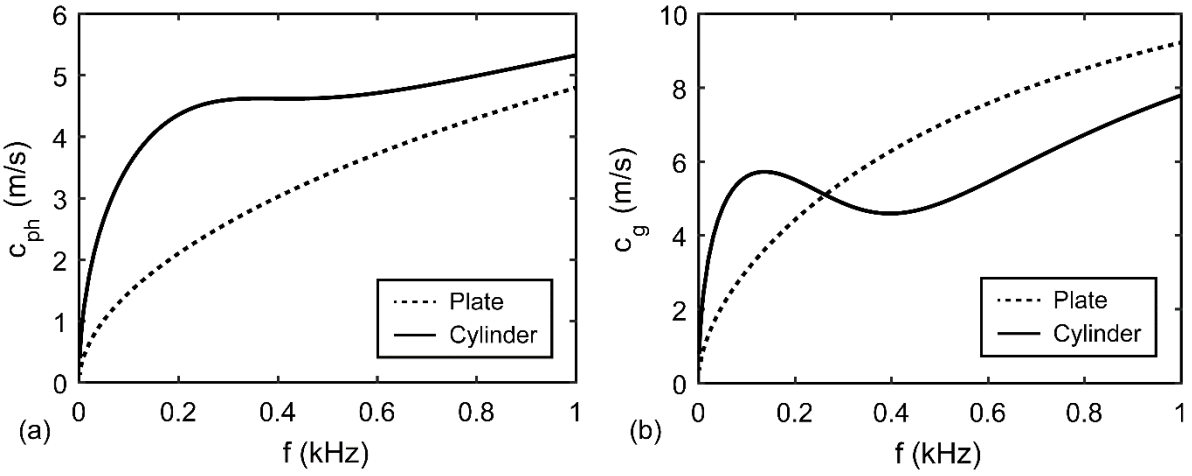

Figure 4 (a) Phase velocity, and (b) group velocity curves obtained by the Fourier-Spectral SAFE model in Figure 3 (b) for the cylindrical waveguide compared with the immersed plate waveguide.

For the SAFE model, the two-dimensional discretization is performed using a mesh similar to that shown in Figure 2 (b) but for a perfect circular cross-section. The solid circular cross-section is discretized using 2 and 32 quadratic elements in the radial and azimuthal directions, respectively. We also used 6 PMDL elements in each stretch direction to model the exterior fluid.

In contrast to SAFE models which are eigenvalue problems in the frequency domain, the 3D FE model, which is borrowed from [55], involves simulation of the actual experiment in the time-domain. As shown in Figure 1(a), in the 3D FE model, the tube is (virtually) excited with a pulse that mimics the radiation force on the surface and the radial component of the displacement is recorded along a line of 220 points with spacing Δz = 0.18018 mm over a time window of t = 0-8 ms with Δt = 0.04 ms. The obtained displacement contour in space-time domain is shown in Figure 5. The dispersion curves are then obtained by performing Fourier transform followed by peak-picking as shown in Figure 1.

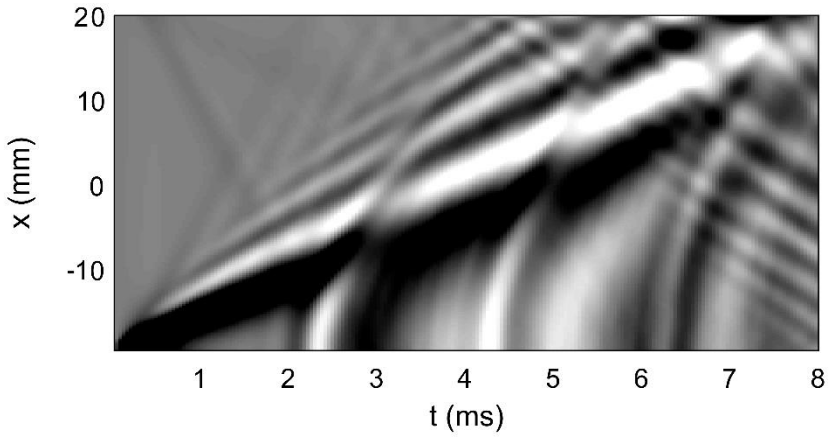

Figure 5 Time-space displacement contour using the 3D model in Figure 3 (a).

The verification is performed in two separate steps: (a) consistency between SAFE (Section 3.3) and Fourier-Spectral SAFE (Section 4) models for cylindrical waveguides, and (b) consistency between Fourier-Spectral SAFE and 3D FEM.

Consistency between results from SAFE and Fourier-Spectral SAFE: Figure 6 contains a comparison of dispersion curves computed using the two approaches. Note that the SAFE model simultaneously retrieves all the wavemodes corresponding to all the circumferential Fourier numbers, to the extent they are resolved by the discretization. For the sake of clarity, in Figure 6, we only show the first mode associated with each circumferential order $n = 0, \cdots, 6$. The figure clearly shows a good match between Fourier-Spectral SAFE and SAFE models, indicating the effectiveness of the proposed Fourier-Spectral SAFE model in predicting the complicated wave dispersion properties.

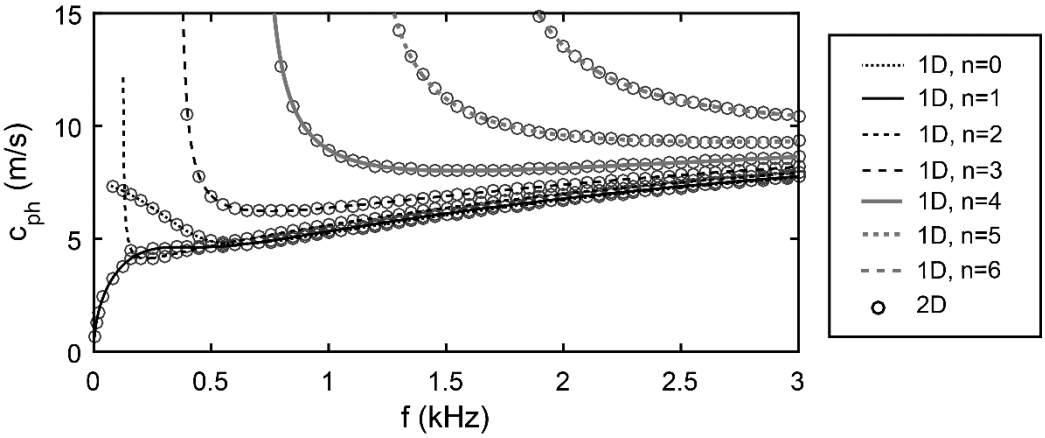

Figure 6 Phase velocity curves obtained by the Fourier-Spectral SAFE model (Figure 3 (b)), and the SAFE model (Figure 2 with cylindrical cross-section).

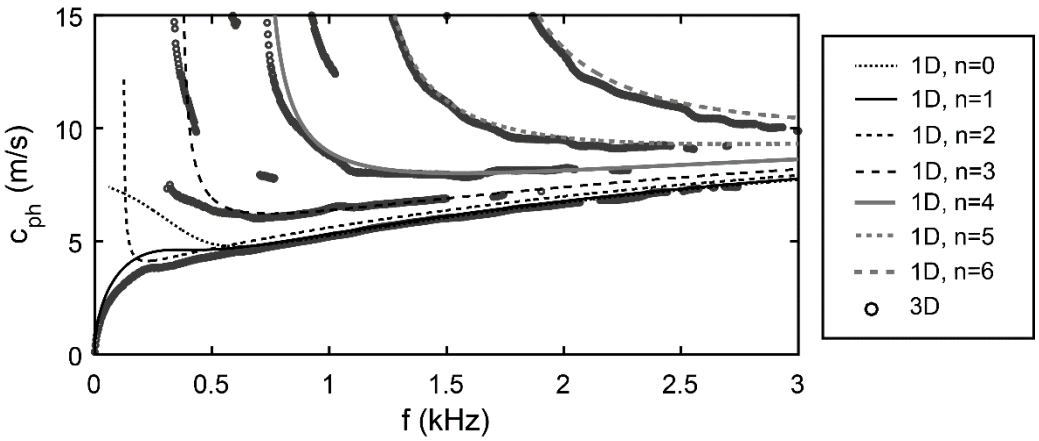

Figure 7 Phase velocity curves obtained by the Fourier-Spectral SAFE model (Figure 3 (b)) and the 3D FE model (Figure 3 (a)). The slight discrepancy is attributed to the errors in the 3D analysis due to, e.g. discretization and boundary conditions.

Consistency between Fourier-Spectral SAFE and 3D FEM: Figure 7 shows the comparison between the dispersion curves extracted from the time-domain simulation with the 3D FE model and the proposed Fourier-Spectral SAFE model. Again, a good match is observed indicating the accuracy of the significantly simpler and more efficient Fourier-Spectral SAFE model. In fact, the Fourier-Spectral SAFE method appears to suffer less from discretization errors, while we suspect that the 3D FE model's non-smooth dispersion curves are a result of errors from discretization, imperfect absorbing boundary conditions, and the fact that not all modes may be sufficiently excited by the radiation force at all the frequencies.

6. Validation

To validate the Fourier-Spectral SAFE model, we consider phantom SWE experiments on fluid-filled, immersed rubber tubes and show that the dispersion curves predicted from the proposed model match closely with the experimental dispersion curves.

Three sets of tubes were made with outer diameters of 8 mm and wall thicknesses of 1 mm to mimic an adult carotid artery. A different rubber mixture was used for each set of tubes, VytaFlex 10 (V10), VytaFlex20 (V20), and ReoFlex 30 (R30) (Smooth-On, Inc., Macungie, PA). SWE measurements were made with a Verasonics system (V1, Verasonics, Inc., Kirkland, WA) and a linear array transducer (L7-4, Philips Healthcare, Andover, MA) in a degassed water tank with water inside and surrounding the tubes. Acoustic radiation force was used to generate the waves with a 200 μs push at 4.09 MHz and plane wave imaging at a frame rate of 14.925 kHz was used for measuring the propagating waves.

Three samples from each mixture were poured for testing with the Hyper-Frequency Viscoelastic Spectroscopy (HFVS) instrument [76]. Figure 8 shows the mean storage (G') and loss modulus (G'') values of the entire measurements. The densities of the urethane rubbers V10, V20, and R30 are reported as 1000, 1000, and 1010 kg/m^3 respectively.

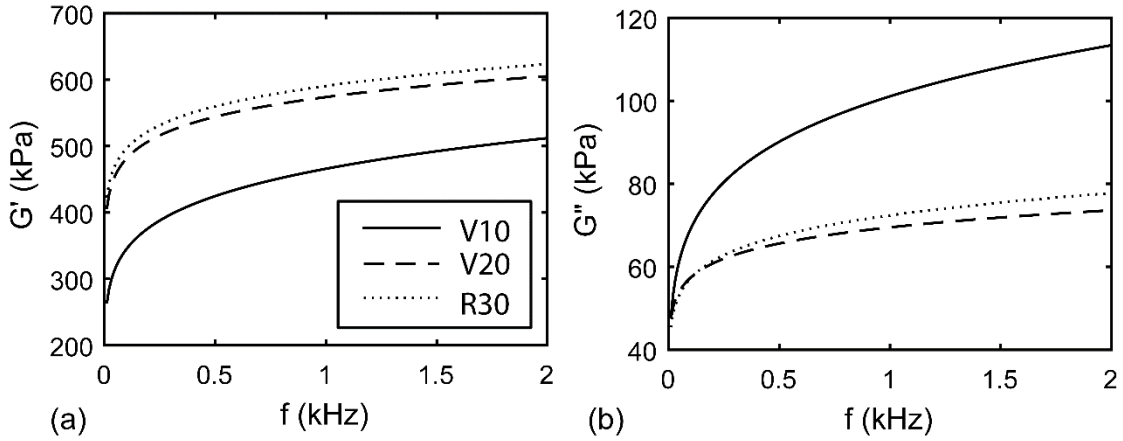

Figure 8 (a) Storage and (b) loss modulus for VytaFlex 10 (V10), VytaFlex20 (V20), and ReoFlex 30 (R30) materials.

The vertical component of the velocity with respect to the ultrasound transducer was recorded along a linear array of 128 elements with a reconstructed spatial sampling of Δx = 0.154 mm over a time window of t = 0-13 ms with Δt = 0.067 ms. We repeated the experiment five times and extracted the experimental dispersion curves by the procedure discussed in Figure 1.

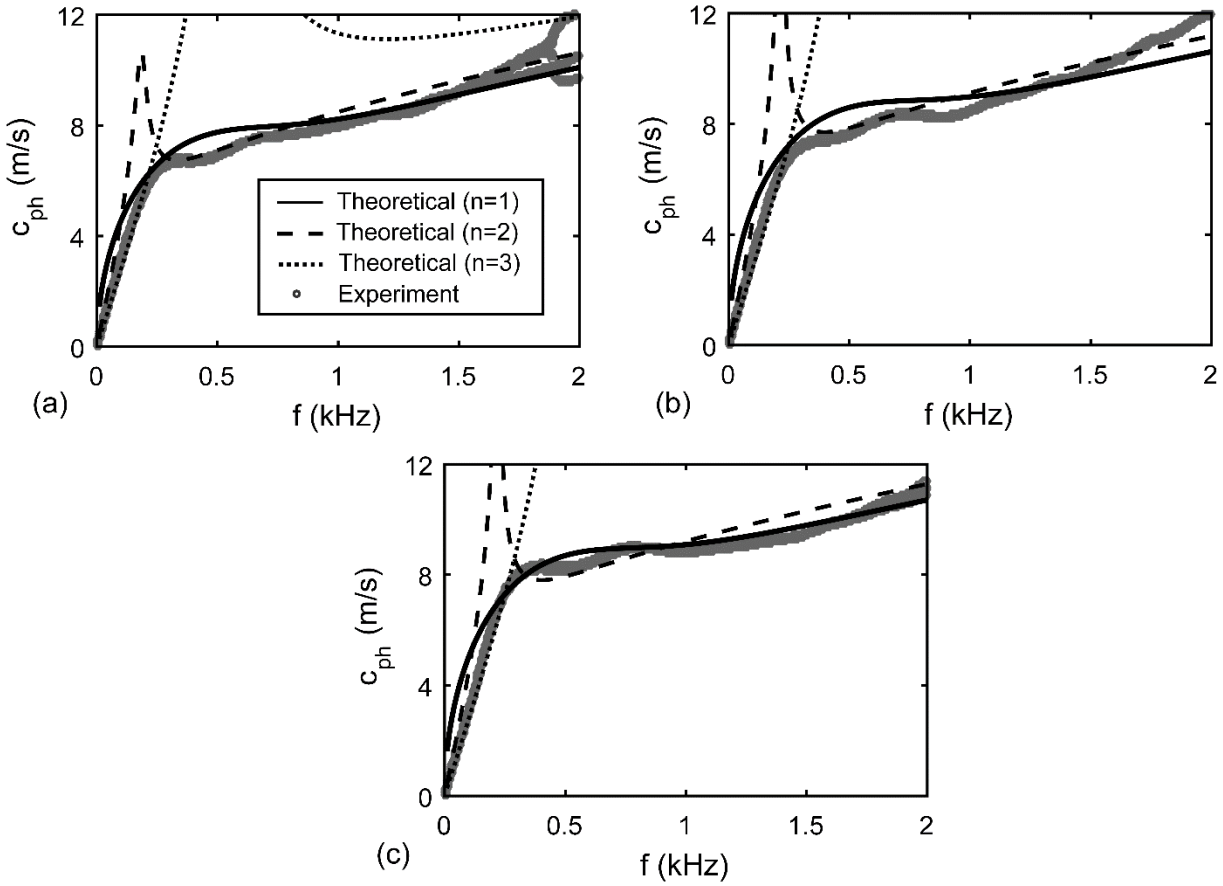

Figure 9 Viscoelastic 1D model (for $n = 1,2,3$) compared with experimental results for (a) VytaFlex 10 (V10), VytaFlex20 (V20), and (c) ReoFlex 30 (R30) rubber tubes.

Figure 9 compares the result of the experiments with the theoretical predication using the measured viscoelastic material properties $(G = G' + iG'')$. Theoretical dispersion curves for flexural modes with circumferential wavenumber $n = 1, 2, 3$ were calculated from the material properties measured with HFVS. The theoretical curves generated using HFVS data show a good agreement with the measured wave propagation results. We emphasize that taking into account the viscoelasticity (frequency dependent and complex shear modulus) of the rubber tubes is crucial to matching the theoretical and experiential curves. Besides, pronounced viscoelastic response of animal and human arteries has been observed in many studies (see e.g. [77-83]).

6.1 Important implication: multimodal dispersion curves

An outcome of the current study is that the experimental dispersion curve is a superposition of multiple theoretical dispersion curves, as opposed to a single theoretical dispersion curve. While it is tempting to think that the main dispersion curve is the dispersion curve associated with the first fundamental mode $(n = 1)$, this is not always the case. Depending on the frequency, higher modes $(n > 1)$ may have larger contribution. Thus higher modes can no longer be neglected; the dispersion curve obtained from the experiment would traverse around the fundamental and higher order modes. This is referred to *effective* dispersion curve (also see [66]) and has important implication with respect to inversion; incorrectly matching to single theoretical dispersion curve could lead to erroneous estimates of the arterial wall properties.

While in this specific example, we noticed that the experimental curve overlapped with three different theoretical dispersion curves, it is possible that the number of involved theoretical curves may not be three, and would depend on the frequency range of observation and potentially the characteristics of the ARF excitation. Careful parametric study would be needed to determine and include all significant theoretical dispersion curves, before robust inversion can be performed.

7. Sensitivity studies

Effect of material properties: Since the eventual goal of SWE is the inversion for the properties of the arterial wall, we perform sensitivity analyses with respect to influential parameters, i.e. shear modulus, wall thickness and internal radius. We consider the tube with properties mentioned in Section 5. For the first mode with circumferential Fourier number $n = 1$, sensitivity of the dispersion curve to these parameters are studied in Figure 10. Note that while changing each parameter, the other two are kept constant at the default values used in Section 5, namely $G = 157\,\text{kPa}$, $h = 1$ mm and $r_{\text{in}} = 3\,\text{mm}$. It is evident from this study that the shear modulus and wall thickness play a more significant role than the internal radius of the tube. The sensitivity to modulus and thickness, while not surprising, confirms that SWE could lead to estimation of these two parameters, which appear to be more important biomarkers [22, 50, 55].

Effect of arterial cross section: The artery may sometimes not be cylindrical due to non-uniform thickening or accumulation of plaque. To examine the effect of non-uniform wall thickness, Figure 11 compares the dispersion curves for the tubes with cylindrical and non-cylindrical cross-sections (both filled with and immersed in fluid). Note that the fundamental flexural mode of the cylindrical tube with circumferential number $n = 1$, converts to two branches for the non-cylindrical tube, which is attributed to the break in axisymmetry. These modes are known as fast and slow fundamental flexural modes and the branching is due to asymmetry of the cross-section (see e.g. [84]). It can also be observed that the higher modes are much more sensitive than the fundamental mode.

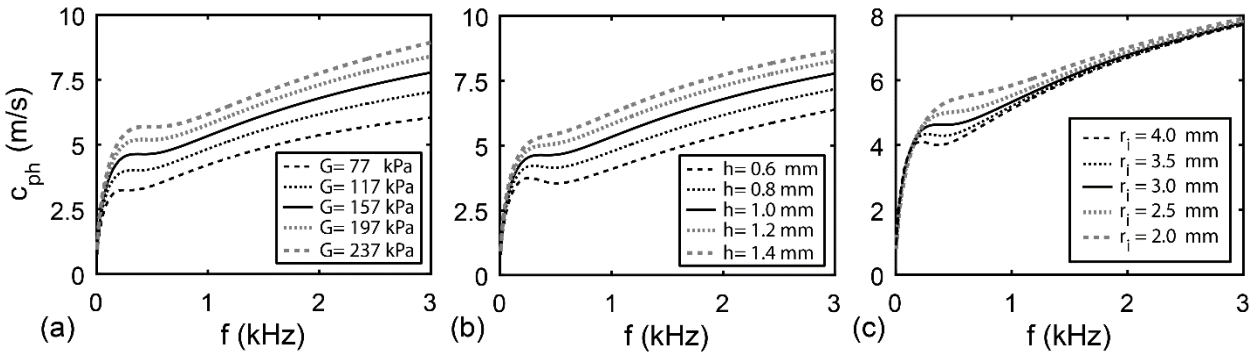

Figure 10 Sensitivity study of tube dispersion curve with respect to (a) shear modulus, (b) thickness, and (c) internal radius. The default parameters for these simulations were $G = 157\text{kPa}$, $h = 1\text{mm}$ and $r_{\text{in}} = 3\text{mm}$.

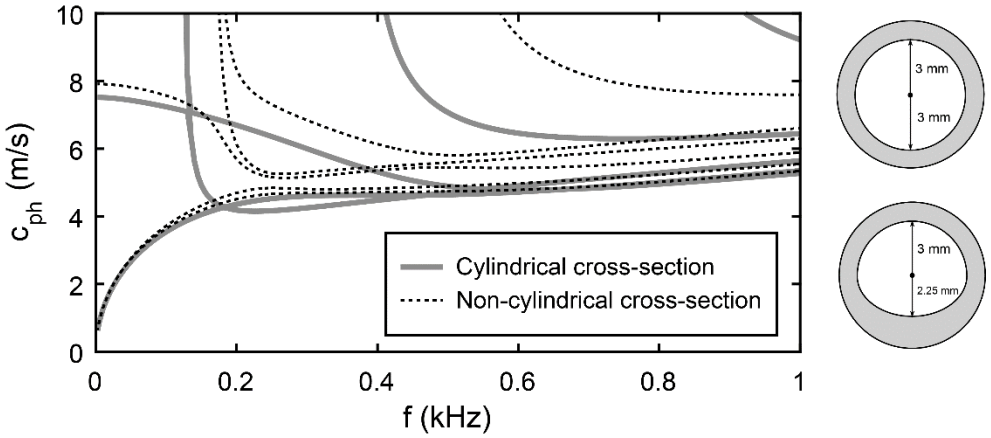

Figure 11 Phase velocity curves obtained by 2D model for (a) cylindrical, and (b) non-cylindrical tubes.

8. Discussion and Conclusion

Towards the final goal of estimating local arterial stiffness from observed guided wave dispersion, we developed efficient models for computing dispersion curves embedded and immersed tubes. In contrast with regular finite element discretization in all three spatial directions, we utilize the semi-analytical finite element (SAFE) method to reduce the problem into two-dimensional eigenvalue problem. In addition, we utilize the cylindrical nature of arteries to further reduce the computational cost by judiciously combining Fourier series in azimuthal direction and high order finite elements in the radial direction. In addition, we have utilized a recently developed method of perfectly matched discrete layers to capture the effect of surrounding fluid. The resulting method, named Fourier-Spectral SAFE method, captures fully three-dimensional wave propagation characteristics with less than 2 seconds on a regular desktop computer (as opposed to 3D FE model, which takes 6 minutes on a 48-processor parallel computer). Such a drastic reduction in computational cost is encouraging because, with further code optimization, it could lead to real-time prediction of arterial stiffness, which would be significant in clinical settings.

The Fourier-Spectral SAFE method for cylindrical waveguides, as well as a 2D SAFE method applicable for non-cylindrical waveguides, are implemented in open-source software WaveDisp [60]. These methods are verified by comparing with much more expensive, fully 3D FE models, clearly

indicating the effectiveness of the proposed methods. Finally, we validated the proposed methods with SWE experiments on tissue-mimicking phantoms, where a close match is observed between experimental and computed dispersion curves.

An important observation from the validation study is that *the experimentally observed dispersion curve does not just match with a single analytical dispersion curve. Instead, it is an overlap of three different analytical dispersion curves*, especially in the lower frequency range. The studies thus far invert for arterial stiffness by matching with single theoretical dispersion curve (see e.g. [22, 49, 50, 52]). In light of our observation, it appears crucial to match with multiple dispersion curves instead, especially because *in vivo* data may be more reliable at lower frequencies.

While the presented results show promise for the proposed methods, much work remains to be done building on this foundation. The next steps include (a) *ex vivo* validation for real arteries, which may require some uncertainty quantification, (b) development of inversion algorithm to estimate arterial stiffness, followed by (c) corroboration with other methods to measure arterial stiffness, and (d) clinical trials.

Acknowledgements

The work is partially funded by National Science Foundation Grants DMS-1016514, CMMI-1635291, and research support from the Mayo Clinic Research Committee.

References

[1] K.-S. Cheng, C. Baker, G. Hamilton, A. Hoeks, A. Seifalian, Arterial elastic properties and cardiovascular risk/event, European journal of vascular and endovascular surgery 24(5) (2002) 383-397.
[2] E. Dolan, L. Thijs, Y. Li, N. Atkins, P. McCormack, S. McClory, E. O'Brien, J.A. Staessen, A.V. Stanton, Ambulatory arterial stiffness index as a predictor of cardiovascular mortality in the Dublin Outcome Study, Hypertension 47(3) (2006) 365-370.
[3] B.A. Kingwell, C.D. Gatzka, Arterial stiffness and prediction of cardiovascular risk, Journal of hypertension 20(12) (2002) 2337-2340.
[4] S. Laurent, P. Boutouyrie, R. Asmar, I. Gautier, B. Laloux, L. Guize, P. Ducimetiere, A. Benetos, Aortic stiffness is an independent predictor of all-cause and cardiovascular mortality in hypertensive patients, Hypertension 37(5) (2001) 1236-1241.
[5] K. Sutton-Tyrrell, S.S. Najjar, R.M. Boudreau, L. Venkitachalam, V. Kupelian, E.M. Simonsick, R. Havlik, E.G. Lakatta, H. Spurgeon, S. Kritchevsky, Elevated aortic pulse wave velocity, a marker of arterial stiffness, predicts cardiovascular events in well-functioning older adults, Circulation 111(25) (2005) 3384-3390.
[6] D.M. Dumont, J.R. Doherty, G.E. Trahey, Noninvasive assessment of wall-shear rate and vascular elasticity using combined ARFI/SWEI/spectral Doppler imaging system, Ultrasonic imaging 33(3) (2011) 165-188.
[7] U. Quinn, L.A. Tomlinson, J.R. Cockcroft, Arterial stiffness, JRSM cardiovascular disease 1(6) (2012) 18.
[8] C. Vlachopoulos, K. Aznaouridis, C. Stefanadis, Prediction of cardiovascular events and all-cause mortality with arterial stiffness: a systematic review and meta-analysis, Journal of the American College of Cardiology 55(13) (2010) 1318-1327.

[9] T. Hirai, S. Sasayama, T. Kawasaki, S. Yagi, Stiffness of systemic arteries in patients with myocardial infarction. A noninvasive method to predict severity of coronary atherosclerosis, Circulation 80(1) (1989) 78-86.
[10] A.P. Guerin, J. Blacher, B. Pannier, S.J. Marchais, M.E. Safar, G.M. London, Impact of aortic stiffness attenuation on survival of patients in end-stage renal failure, Circulation 103(7) (2001) 987-992.
[11] J.R. Cockcroft, I.B. Wilkinson, M. Evans, P. McEwan, J.R. Peters, S. Davies, M.F. Scanlon, C.J. Currie, Pulse pressure predicts cardiovascular risk in patients with type 2 diabetes mellitus, American journal of hypertension 18(11) (2005) 1463-1467.
[12] C. Bussy, P. Boutouyrie, P. Lacolley, P. Challande, S. Laurent, Intrinsic stiffness of the carotid arterial wall material in essential hypertensives, Hypertension 35(5) (2000) 1049-1054.
[13] P. Lacolley, S. Laurent, Aortic Stiffness Is an Independent Predictor of Primary Coronary Events in Hypertensive Patients a longitudinal study, Hypertension 39(1) (2002) 10-15.
[14] A. Paini, P. Boutouyrie, D. Calvet, A.-I. Tropeano, B. Laloux, S. Laurent, Carotid and aortic stiffness determinants of discrepancies, Hypertension 47(3) (2006) 371-376.
[15] S.P. Glasser, D.K. Arnett, G.E. McVeigh, S.M. Finkelstein, A.J. Bank, D.J. Morgan, J.N. Cohn, Vascular compliance and cardiovascular disease: a risk factor or a marker?, American Journal of Hypertension 10(10) (1997) 1175-1189.
[16] J.J. Oliver, D.J. Webb, Noninvasive assessment of arterial stiffness and risk of atherosclerotic events, Arteriosclerosis, Thrombosis, and Vascular Biology 23(4) (2003) 554-566.
[17] P. Boutouyrie, S. Laurent, A. Benetos, X.J. Girerd, A.P. Hoeks, M.E. Safar, Opposing effects of ageing on distal and proximal large arteries in hypertensives, Journal of Hypertension 10 (1992) S87-S92.
[18] L.M. Van Bortel, S. Laurent, P. Boutouyrie, P. Chowienczyk, J. Cruickshank, T. De Backer, J. Filipovsky, S. Huybrechts, F.U. Mattace-Raso, A.D. Protogerou, Expert consensus document on the measurement of aortic stiffness in daily practice using carotid-femoral pulse wave velocity, Journal of hypertension 30(3) (2012) 445-448.
[19] C. Caro, G.K. HARRISON, Observations on pulse wave velocity and pulsatile blood pressure in the human pulmonary circulation, Clinical science 23 (1962) 317.
[20] R. Asmar, A. Benetos, J. Topouchian, P. Laurent, B. Pannier, A.-M. Brisac, R. Target, B.I. Levy, Assessment of arterial distensibility by automatic pulse wave velocity measurement validation and clinical application studies, Hypertension 26(3) (1995) 485-490.
[21] A. Mookerjee, A.M. Al-Jumaily, A. Lowe, Arterial pulse wave velocity measurement: different techniques, similar results—implications for medical devices, Biomechanics and modeling in mechanobiology 9(6) (2010) 773-781.
[22] M. Bernal, I. Nenadic, M.W. Urban, J.F. Greenleaf, Material property estimation for tubes and arteries using ultrasound radiation force and analysis of propagating modes, The Journal of the Acoustical Society of America 129(3) (2011) 1344-1354.
[23] M. Couade, M. Pernot, C. Prada, E. Messas, J. Emmerich, P. Bruneval, A. Criton, M. Fink, M. Tanter, Quantitative assessment of arterial wall biomechanical properties using shear wave imaging, Ultrasound in medicine & biology 36(10) (2010) 1662-1676.
[24] D. Korteweg, Ueber die Fortpflanzungsgeschwindigkeit des Schalles in elastischen Röhren, Annalen der Physik 241(12) (1878) 525-542.
[25] F. van den Berkmortel, M. Van Der Steen, H. Hoogenboom, H. Wollersheim, H. Van Langen, T. Thien, Progressive arterial wall stiffening in patients with increasing diastolic blood pressure, Journal of human hypertension 15(10) (2001).
[26] F. Viola, M.D. Kramer, M.B. Lawrence, J.P. Oberhauser, W.F. Walker, Sonorheometry: a noncontact method for the dynamic assessment of thrombosis, Annals of biomedical engineering 32(5) (2004) 696-705.
[27] K. Nightingale, M.S. Soo, R. Nightingale, G. Trahey, Acoustic radiation force impulse imaging: in vivo demonstration of clinical feasibility, Ultrasound in medicine & biology 28(2) (2002) 227-235.

[28] A.P. Sarvazyan, O.V. Rudenko, S.D. Swanson, J.B. Fowlkes, S.Y. Emelianov, Shear wave elasticity imaging: a new ultrasonic technology of medical diagnostics, Ultrasound in medicine & biology 24(9) (1998) 1419-1435.
[29] J. Bercoff, M. Tanter, M. Fink, Supersonic shear imaging: a new technique for soft tissue elasticity mapping, IEEE transactions on ultrasonics, ferroelectrics, and frequency control 51(4) (2004) 396-409.
[30] T. Deffieux, G. Montaldo, M. Tanter, M. Fink, Shear wave spectroscopy for in vivo quantification of human soft tissues visco-elasticity, IEEE transactions on medical imaging 28(3) (2009) 313-322.
[31] S.A. McAleavey, M. Menon, J. Orszulak, Shear-modulus estimation by application of spatially-modulated impulsive acoustic radiation force, Ultrasonic imaging 29(2) (2007) 87-104.
[32] M. Fatemi, J.F. Greenleaf, Ultrasound-stimulated vibro-acoustic spectrography, Science 280(5360) (1998) 82-85.
[33] E.E. Konofagou, K. Hynynen, Localized harmonic motion imaging: theory, simulations and experiments, Ultrasound in medicine & biology 29(10) (2003) 1405-1413.
[34] Z. Hah, C. Hazard, Y.T. Cho, D. Rubens, K. Parker, Crawling waves from radiation force excitation, Ultrasonic imaging 32(3) (2010) 177-189.
[35] S. Chen, M. Fatemi, J.F. Greenleaf, Quantifying elasticity and viscosity from measurement of shear wave speed dispersion, The Journal of the Acoustical Society of America 115(6) (2004) 2781-2785.
[36] S. Chen, M.W. Urban, C. Pislaru, R. Kinnick, Y. Zheng, A. Yao, J.F. Greenleaf, Shearwave dispersion ultrasound vibrometry (SDUV) for measuring tissue elasticity and viscosity, IEEE transactions on ultrasonics, ferroelectrics, and frequency control 56(1) (2009) 55-62.
[37] J.R. Doherty, G.E. Trahey, K.R. Nightingale, M.L. Palmeri, Acoustic radiation force elasticity imaging in diagnostic ultrasound, IEEE transactions on ultrasonics, ferroelectrics, and frequency control 60(4) (2013) 685-701.
[38] C. Amador, M.W. Urban, S. Chen, J.F. Greenleaf, Shearwave dispersion ultrasound vibrometry (SDUV) on swine kidney, IEEE transactions on ultrasonics, ferroelectrics, and frequency control 58(12) (2011) 2608-2619.
[39] F.G. Mitri, M.W. Urban, M. Fatemi, J.F. Greenleaf, Shear wave dispersion ultrasonic vibrometry for measuring prostate shear stiffness and viscosity: an in vitro pilot study, IEEE transactions on biomedical engineering 58(2) (2011) 235-242.
[40] I.Z. Nenadic, B. Qiang, M.W. Urban, L.H. de Araujo Vasconcelo, A. Nabavizadeh, A. Alizad, J.F. Greenleaf, M. Fatemi, Ultrasound bladder vibrometry method for measuring viscoelasticity of the bladder wall, Physics in medicine and biology 58(8) (2013) 2675.
[41] X. Zhang, R.R. Kinnick, M. Fatemi, J.F. Greenleaf, Noninvasive method for estimation of complex elastic modulus of arterial vessels, IEEE transactions on ultrasonics, ferroelectrics, and frequency control 52(4) (2005) 642-652.
[42] J.-L. Gennisson, T. Deffieux, E. Macé, G. Montaldo, M. Fink, M. Tanter, Viscoelastic and anisotropic mechanical properties of in vivo muscle tissue assessed by supersonic shear imaging, Ultrasound in medicine & biology 36(5) (2010) 789-801.
[43] D. Shcherbakova, C. Papadacci, A. Swillens, A. Caenen, S. De Bock, V. Saey, K. Chiers, M. Tanter, S. Greenwald, M. Pernot, Supersonic shear wave imaging to assess arterial nonlinear behavior and anisotropy: proof of principle via ex vivo testing of the horse aorta, Advances in Mechanical Engineering 6 (2014) 272586.
[44] T. Kundu, Ultrasonic nondestructive evaluation: engineering and biological material characterization, CRC press, Boca Raton, FL, 2003.
[45] J.L. Rose, Ultrasonic guided waves in solid media, Cambridge University Press, New York, NY, 2014.
[46] J.-k. Jang, K. Kondo, T. Namita, M. Yamakawa, T. Shiina, Comparison of techniques for estimating shear-wave velocity in arterial wall using shear-wave elastography-FEM and phantom study, Ultrasonics Symposium (IUS), 2015 IEEE International, IEEE, 2015, pp. 1-4.

[47] E. Widman, E. Maksuti, C. Amador, M.W. Urban, K. Caidahl, M. Larsson, Shear Wave Elastography Quantifies Stiffness in Ex Vivo Porcine Artery with Stiffened Arterial Region, Ultrasound in Medicine & Biology 42(10) (2016) 2423-2435.
[48] T.-m. Nguyen, M. Couade, J. Bercoff, M. Tanter, Assessment of viscous and elastic properties of sub-wavelength layered soft tissues using shear wave spectroscopy: theoretical framework and in vitro experimental validation, IEEE transactions on ultrasonics, ferroelectrics, and frequency control 58(11) (2011) 2305-2315.
[49] E. Widman, E. Maksuti, D. Larsson, M.W. Urban, A. Bjällmark, M. Larsson, Shear wave elastography plaque characterization with mechanical testing validation: a phantom study, Physics in medicine and biology 60(8) (2015) 3151.
[50] E. Maksuti, E. Widman, D. Larsson, M.W. Urban, M. Larsson, A. Bjällmark, Arterial Stiffness Estimation by Shear Wave Elastography: Validation in Phantoms with Mechanical Testing, Ultrasound in medicine & biology 42(1) (2016) 308-321.
[51] G.-Y. Li, Q. He, G. Xu, L. Jia, J. Luo, Y. Cao, An ultrasound elastography method to determine the local stiffness of arteries with guided circumferential waves, Journal of Biomechanics 51 (2017) 97-104.
[52] G.-Y. Li, Q. He, L. Jia, P. He, J. Luo, Y. Cao, An Inverse Method to Determine Arterial Stiffness with Guided Axial Waves, Ultrasound in Medicine & Biology 43(2) (2016) 505–516
[53] V. Flamini, A.P. Creane, C.M. Kerskens, C. Lally, Imaging and finite element analysis: a methodology for non-invasive characterization of aortic tissue, Medical engineering & physics 37(1) (2015) 48-54.
[54] S.-M. Lin, W.-R. Wang, S.-Y. Lee, C.-W. Chen, Y.-C. Hsiao, M.-J. Teng, Wave modes of a pre-stressed thick tube conveying blood on the viscoelastic foundation, Applied Mathematical Modelling 39(2) (2015) 466-482.
[55] P. Dutta, M.W. Urban, O.P. Le Maitre, J.F. Greenleaf, W. Aquino, Simultaneous identification of elastic properties, thickness, and diameter of arteries excited with ultrasound radiation force, Physics in Medicine and Biology 60(13) (2015) 5279-5296.
[56] V.C. Protopappas, I.C. Kourtis, L.C. Kourtis, K.N. Malizos, C.V. Massalas, D.I. Fotiadis, Three-dimensional finite element modeling of guided ultrasound wave propagation in intact and healing long bones, Journal of the Acoustical Society of America 121(6) (2007) 3907-3921.
[57] D. Ta, W.Q. Wang, Y.Y. Wang, L.H. Le, Y.Q. Zhou, Measurement of the dispersion and attenuation of cylindrical ultrasonic guided waves in long bone, Ultrasound in Medicine and Biology 35(4) (2009) 641-652.
[58] K.L. Xu, D.A. Ta, W.Q. Wang, Multiridge-Based Analysis for Separating Individual Modes From Multimodal Guided Wave Signals in Long Bones, Ieee Transactions on Ultrasonics Ferroelectrics and Frequency Control 57(11) (2010) 2480-2490.
[59] J.G. Chen, Z.Q. Su, On ultrasound waves guided by bones with coupled soft tissues: A mechanism study and in vitro calibration, Ultrasonics 54(5) (2014) 1186-1196.
[60] A. Vaziri Astaneh, M.N. Guddati, WaveDisp software. <http://WaveDisp.com>).
[61] J.L. Tassoulas, E. Kausel, Elements for the numerical-analysis of wave motion in layered strata, International Journal for Numerical Methods in Engineering 19(7) (1983) 1005-1032.
[62] A. Vaziriastaneh, On the forward and inverse computational wave propagation problems, PhD Thesis, North Carolina State University, USA, 2016.
[63] M.N. Guddati, K.W. Lim, Continued fraction absorbing boundary conditions for convex polygonal domains, International Journal for Numerical Methods in Engineering 66(6) (2006) 949-977.
[64] M.N. Guddati, K.W. Lim, M.A. Zahid, Perfectly matched discrete layers for unbounded domain modeling, in: F. Magoulès (Ed.), Computational methods for acoustics problems, Saxe-Coburg Publications, UK, 2008, pp. 69-98.
[65] W.C. Chew, W.H. Weedon, A 3d perfectly matched medium from modified maxwells equations with stretched coordinates, Microwave and Optical Technology Letters 7(13) (1994) 599-604.
[66] A. Vaziri Astaneh, M.N. Guddati, Improved Inversion Algorithms for Near Surface Characterization, Geophysical Journal International 206(2) (2016) 1410-1423.

[67] C. Bonithon-Kopp, P.-J. Touboul, C. Berr, C. Leroux, F. Mainard, D. Courbon, P. Ducimetière, Relation of intima-media thickness to atherosclerotic plaques in carotid arteries, Arteriosclerosis, thrombosis, and vascular biology 16(2) (1996) 310-316.
[68] M. Zureik, P. Ducimetiere, P.-J. Touboul, D. Courbon, C. Bonithon-Kopp, C. Berr, C. Magne, Common carotid intima-media thickness predicts occurrence of carotid atherosclerotic plaques, Arteriosclerosis, thrombosis, and vascular biology 20(6) (2000) 1622-1629.
[69] C. Glorieux, K. Van de Rostyne, K. Nelson, W.M. Gao, W. Lauriks, J. Thoen, On the character of acoustic waves at the interface between hard and soft solids and liquids, Journal of the Acoustical Society of America 110(3) (2001) 1299-1306.
[70] P.C. Vinh, Scholte-wave velocity formulae, Wave Motion 50(2) (2013) 180-190.
[71] G.A. Holzapfel, R.W. Ogden, Constitutive modelling of arteries, Proceedings of the Royal Society of London A: Mathematical, Physical and Engineering Sciences 466(2118) (2010) 1551-1597.
[72] P. Kalita, R. Schaefer, Mechanical models of artery walls, Archives of Computational Methods in Engineering 15(1) (2008) 1-36.
[73] J. Humphrey, G.A. Holzapfel, Mechanics, mechanobiology, and modeling of human abdominal aorta and aneurysms, Journal of biomechanics 45(5) (2012) 805-814.
[74] J. Humphrey, J. Wilson, Arteries: Mechanics, Mechanobiology, and the Need for a New Class of Models, Multiscale Modeling in Biomechanics and Mechanobiology, Springer2015, pp. 207-222.
[75] T.C. Gasser, R.W. Ogden, G.A. Holzapfel, Hyperelastic modelling of arterial layers with distributed collagen fibre orientations, Journal of the royal society interface 3(6) (2006) 15-35.
[76] A.H. Henni, C. Schmitt, M.-É. Tremblay, M. Hamdine, M.-C. Heuzey, P. Carreau, G. Cloutier, Hyper-frequency viscoelastic spectroscopy of biomaterials, Journal of the mechanical behavior of biomedical materials 4(7) (2011) 1115-1122.
[77] H. Abé, K. Hayashi, M. Sato, Data book on mechanical properties of living cells, tissues, and organs, Springer, Japan, 1996.
[78] D. Valdez-Jasso, D. Bia, Y. Zócalo, R.L. Armentano, M.A. Haider, M.S. Olufsen, Linear and nonlinear viscoelastic modeling of aorta and carotid pressure–area dynamics under in vivo and ex vivo conditions, Annals of biomedical engineering 39(5) (2011) 1438-1456.
[79] Y.-C. Fung, Biomechanics: mechanical properties of living tissues, Springer Science & Business Media, New York, NY, 1993.
[80] X.-F. Wanga, J.-M. Fullana, P.-Y. Lagrée, R. Armentano, Effect of viscoelasticity of arterial wall on pulse wave: a comparative study on ovine, Computer methods in biomechanics and biomedical engineering 16(sup1) (2013) 25-26.
[81] R.L. Armentano, D.B. Santana, E.I.C. Fischer, S. Graf, H.P. Cámpos, Y.Z. Germán, M. del Carmen Saldías, I. Alvarez, An in vitro study of cryopreserved and fresh human arteries: a comparison with ePTFE prostheses and human arteries studied non-invasively in vivo, Cryobiology 52(1) (2006) 17-26.
[82] J. Peña, M. Martínez, E. Peña, A formulation to model the nonlinear viscoelastic properties of the vascular tissue, Acta Mechanica 217(1-2) (2011) 63-74.
[83] A. Lundkvist, E. Lilleodden, W. Siekhaus, J. Kinney, L. Pruitt, M. Balooch, Viscoelastic properties of healthy human artery measured in saline solution by AFM-based indentation technique, MRS Proceedings, Cambridge Univ Press, 1996, p. 353.
[84] M. Mazzotti, I. Bartoli, A. Marzani, Ultrasonic leaky guided waves in fluid-coupled generic waveguides: hybrid finite-boundary element dispersion analysis and experimental validation, Journal of Applied Physics 115(14) (2014) 1-10.

Appendix A: Semi-discretization in 2D Cartesian coordinates (SAFE method)

Expanding the governing equation in (1a) by using (3) gives,

$$
\begin{aligned}
&-\partial(\mathbf{D}_{xx}\partial\mathbf{u}/\partial x)/\partial x-\partial(\mathbf{D}_{xy}\partial\mathbf{u}/\partial y)/\partial x-\partial(\mathbf{D}_{xz}\partial\mathbf{u}/\partial z)/\partial x\\
&-\partial(\mathbf{D}_{xy}^{T}\partial\mathbf{u}/\partial x)/\partial y-\partial(\mathbf{D}_{yy}\partial\mathbf{u}/\partial y)/\partial y-\partial(\mathbf{D}_{yz}\partial\mathbf{u}/\partial z)/\partial y\\
&-\partial(\mathbf{D}_{xz}^{T}\partial\mathbf{u}/\partial x)/\partial z-\partial(\mathbf{D}_{yz}^{T}\partial\mathbf{u}/\partial y)/\partial z-\partial(\mathbf{D}_{zz}\partial\mathbf{u}/\partial z)/\partial z-\rho_S\omega^2\mathbf{I}_{3\times3}\mathbf{u}=\mathbf{0}
\end{aligned}
\tag{A1}
$$

where $\mathbf{D}_{pq}=(\mathbf{L}_p^S)^T\mathbf{D}_{6\times6}\mathbf{L}_q^S$ for $p,q\in\{x,y,z\}$ and $\mathbf{L}^S$ matrices are defined in (3). We use Fourier transform in the z direction and discretize the solid and fluid domains in the $x-y$ plane, i.e. $\mathbf{u}(x,y,z,\omega)=\mathbf{N}_S(x,y)\bar{\mathbf{u}}(k_z,\omega)e^{ik_zz}$ and $p(x,y,z,\omega)=\mathbf{N}_F(x,y)\bar{p}(k_z,\omega)e^{ik_zz}$ where k_z is the axial wavenumber. Shape function matrix is defined as the Kronecker product $\mathbf{N}_S=\bar{\mathbf{N}}_S\otimes\mathbf{I}_{3\times3}$ where $\bar{\mathbf{N}}_S=[N_S^1,...,N_S^{m_S}]$ is the shape function vector for a 2D m_S-noded element in the solid domain and $\mathbf{N}_F=[N_F^1,...,N_F^{m_F}]$ is the shape function vector for a 2D m_F-noded element in the fluid region. The resulting quadratic eigenvalue problem can be written as,

$$
\begin{bmatrix}
k_z^2\tilde{\mathbf{K}}^{S2}+ik_z\tilde{\mathbf{K}}^{S1}+\tilde{\mathbf{K}}^{S0}-\omega^2\tilde{\mathbf{M}}^{S} & -\mathbf{C}_{SF}\\
-\omega^2\mathbf{C}_{SF}^{T} & k_z^2\mathbf{K}^{F2}+\mathbf{K}^{F0}-\omega^2\mathbf{M}^{F}
\end{bmatrix}
\begin{Bmatrix}\tilde{\boldsymbol{\phi}}_S\\ \boldsymbol{\phi}_F\end{Bmatrix}=\begin{Bmatrix}\mathbf{0}\\ \mathbf{0}\end{Bmatrix},
\tag{A2}
$$

where $\tilde{\mathbf{K}}^{S2}=\mathbf{K}_{zz}^S$, $\tilde{\mathbf{K}}^{S1}=\mathbf{K}_{xz}^S-(\mathbf{K}_{xz}^S)^T+\mathbf{K}_{yz}^S-(\mathbf{K}_{yz}^S)^T$, $\tilde{\mathbf{K}}^{S0}=\mathbf{K}_{xx}^S+\mathbf{K}_{yy}^S+\mathbf{K}_{xy}^S+(\mathbf{K}_{xy}^S)^T$, $\mathbf{K}^{F2}=\mathbf{K}_{zz}^F$, and $\mathbf{K}^{F0}=\mathbf{K}_{xy}^F$ with,

$$
\begin{aligned}
&\mathbf{K}_{xx}^S=\int_\Omega\mathbf{B}_{Sx}^T\mathbf{D}_{xx}\mathbf{B}_{Sx}d\Omega, && \mathbf{K}_{xy}^S=\int_\Omega\mathbf{B}_{Sx}^T\mathbf{D}_{xy}\mathbf{B}_{Sy}d\Omega, && \mathbf{K}_{xz}^S=\int_\Omega\mathbf{B}_{Sx}^T\mathbf{D}_{xz}\mathbf{N}_Sd\Omega,\\
&\mathbf{K}_{yy}^S=\int_\Omega\mathbf{B}_{Sy}^T\mathbf{D}_{yy}\mathbf{B}_{Sy}^Td\Omega, && \mathbf{K}_{yz}^S=\int_\Omega\mathbf{B}_{Sy}^T\mathbf{D}_{yz}\mathbf{N}_Sd\Omega, && \mathbf{K}_{zz}^S=\int_\Omega\mathbf{N}_S^T\mathbf{D}_{zz}\mathbf{N}_Sd\Omega,\\
&\mathbf{M}^S=\int_\Omega\mathbf{N}_S^T\rho_S\mathbf{N}_Sd\Omega, && \mathbf{K}_{xy}^F=\int_\Omega\mathbf{B}_F^T\rho_F^{-1}\mathbf{B}_Fd\Omega, && \mathbf{K}_{zz}^F=\int_\Omega\mathbf{N}_F^T\rho_F^{-1}\mathbf{N}_Fd\Omega,\\
&\mathbf{M}^F=\int_\Omega\mathbf{N}_F^T\rho_F^{-1}c_F^{-2}\mathbf{N}_Fd\Omega, && \mathbf{C}_{SF}=\int_\Gamma\mathbf{N}_S^T\mathbf{n}_f\mathbf{N}_Fd\Gamma, &&
\end{aligned}
\tag{A3}
$$

where $\mathbf{B}_{Sx}=\bar{\mathbf{B}}_{Sx}\otimes\mathbf{I}_{3\times3}$, $\mathbf{B}_{Sy}=\bar{\mathbf{B}}_{Sy}\otimes\mathbf{I}_{3\times3}$, $\bar{\mathbf{B}}_{Sx}=[dN_S^1/dx,...,dN_S^{m_S}/dx]$, $\bar{\mathbf{B}}_{Sy}=[dN_S^1/dy,...,dN_S^{m_S}/dy]$ and $\mathbf{B}_F=[dN_F^1/dx,...,dN_F^{m_F}/dx;\ dN_F^1/dy,...,dN_F^{m_F}/dy]$. Also $\mathbf{n}_f=\{n_1\ n_2\ 0\}^T$ is the unit normal for the fluid at each interface. By rearranging the degrees of freedom (x then y and z), the quadratic eigenvalue problem in (A2) can be converted to the generalized eigenvalue problem in (5) with,

$$
\mathbf{K}_2^S=\begin{bmatrix}\tilde{\mathbf{K}}_{xx}^{S2} & \mathbf{0} & -\tilde{\mathbf{K}}_{xz}^{S1}\\ \mathbf{0} & \tilde{\mathbf{K}}_{yy}^{S2} & -\tilde{\mathbf{K}}_{yz}^{S1}\\ \mathbf{0} & \mathbf{0} & \tilde{\mathbf{K}}_{zz}^{S2}\end{bmatrix},\ \mathbf{K}_0^S=\begin{bmatrix}\tilde{\mathbf{K}}_{xx}^{S0} & \tilde{\mathbf{K}}_{xy}^{S0} & \mathbf{0}\\ \tilde{\mathbf{K}}_{yx}^{S0} & \tilde{\mathbf{K}}_{yy}^{S0} & \mathbf{0}\\ \tilde{\mathbf{K}}_{zx}^{S1} & \tilde{\mathbf{K}}_{zy}^{S1} & \tilde{\mathbf{K}}_{zz}^{S0}\end{bmatrix},
\tag{A4}
$$

and $\boldsymbol{\phi}_S=\{ik_z\tilde{\boldsymbol{\phi}}_{Sx}^T\quad ik_z\tilde{\boldsymbol{\phi}}_{Sy}^T\quad\tilde{\boldsymbol{\phi}}_{Sz}^T\}^T$. Note that the size of the generalized eigenvalue problem in (5) is the same as the original quadratic eigenvalue problem in (A2).

Appendix B: Semi-discretization in radial direction (for Fourier-Spectral SAFE method)

Expanding the governing equation in (1a) by using (8) gives,

$$
\begin{aligned}
&-r^{-1}\partial(\mathbf{D}_{rr}r\partial\mathbf{u}/\partial r)/\partial r - r^{-1}\partial(\mathbf{D}_{r\theta}\partial\mathbf{u}/\partial\theta)/\partial r - r^{-1}\partial(\mathbf{D}_{rz}r\partial\mathbf{u}/\partial z)/\partial r - r^{-1}\partial(\mathbf{D}_{ro}\mathbf{u})/\partial r \\
&-r^{-1}\partial(\mathbf{D}_{r\theta}^{T}\partial\mathbf{u}/\partial r)/\partial\theta - r^{-1}\partial(\mathbf{D}_{\theta\theta}r^{-1}\partial\mathbf{u}/\partial\theta)/\partial\theta - r^{-1}\partial(\mathbf{D}_{\theta z}\partial\mathbf{u}/\partial z)/\partial\theta - r^{-1}\partial(\mathbf{D}_{\theta o}r^{-1}\mathbf{u})/\partial\theta \\
&-\partial(\mathbf{D}_{rz}^{T}\partial\mathbf{u}/\partial r)/\partial z - \partial(\mathbf{D}_{\theta z}^{T}r^{-1}\partial\mathbf{u}/\partial\theta)/\partial z - \partial(\mathbf{D}_{zz}\partial\mathbf{u}/\partial z)/\partial z - \partial(\mathbf{D}_{zo}r^{-1}\mathbf{u})/\partial z \\
&+r^{-1}(\mathbf{D}_{ro}^{T})\partial\mathbf{u}/\partial r + r^{-1}(\mathbf{D}_{\theta o}^{T}r^{-1})\partial\mathbf{u}/\partial\theta + r^{-1}(\mathbf{D}_{zo}^{T})\partial\mathbf{u}/\partial z + r^{-1}(\mathbf{D}_{oo}r^{-1})\mathbf{u} - \rho_S\omega^2\mathbf{I}_{3\times3}\mathbf{u} = \mathbf{0}
\end{aligned}
\tag{B1}
$$

where $\mathbf{D}_{pq} = (\mathbf{L}_p^S)^T\mathbf{D}_{6\times6}\mathbf{L}_q^S$ for $p,q\in\{r,\theta,z,o\}$ and $\mathbf{L}^S$ matrices are defined in (8). We use Fourier series in θ, Fourier transform in the z direction, and discretize the solid and fluid domains along the r direction, i.e. $\mathbf{u}(r,\theta,z,\omega) = \mathbf{N}_S(r)\bar{\mathbf{u}}(n,k_z,\omega)e^{in\theta+ik_z z}$ and $p(r,\theta,z,\omega) = \mathbf{N}_F(r)\bar{p}(n,k_z,\omega)e^{in\theta+ik_z z}$ where k_z is the axial wavenumber and n is the circumferential Fourier number. The shape function matrix is defined as the Kronecker product $\mathbf{N}_S = \bar{\mathbf{N}}_S\otimes\mathbf{I}_{3\times3}$ where $\bar{\mathbf{N}}_S = [N_S^1,...,N_S^{m_S}]$ is the shape function vector for a 1D m_S-noded element in the solid domain $(r_1\le r\le r_2)$ and $\mathbf{N}_F = [N_F^1,...,N_F^{m_F}]$ is the shape function vector for a 1D m_F-noded element in the fluid region $(r_2\le r)$. The resulting quadratic eigenvalue problem is similar to (A2) where $\tilde{\mathbf{K}}^{S0} = \mathbf{K}_{rr}^S + \mathbf{K}_{ro}^S + (\mathbf{K}_{ro}^S)^T + \mathbf{K}_{oo}^S + in(\mathbf{K}_{r\theta}^S - (\mathbf{K}_{r\theta}^S)^T + (\mathbf{K}_{\theta o}^S)^T - \mathbf{K}_{\theta o}^S) + n^2\mathbf{K}_{\theta\theta}^S$, $\tilde{\mathbf{K}}^{S2} = \mathbf{K}_{zz}^S$, $\mathbf{K}^{F2} = \mathbf{K}_{zz}^F$, $\mathbf{K}^{F0} = \mathbf{K}_{rr}^F + n^2\mathbf{K}_{\theta\theta}^F$ and $\tilde{\mathbf{K}}^{S1} = \mathbf{K}_{rz}^S - (\mathbf{K}_{rz}^S)^T - \mathbf{K}_{zo}^S + (\mathbf{K}_{zo}^S)^T - in(\mathbf{K}_{\theta z}^S + (\mathbf{K}_{\theta z}^S)^T)$ with,

$$
\begin{aligned}
&\mathbf{K}_{rr}^S = \int_{r_1}^{r_2}\mathbf{B}_S^T\mathbf{D}_{rr}\mathbf{B}_S r dr, \quad \mathbf{K}_{r\theta}^S = \int_{r_1}^{r_2}\mathbf{B}_S^T r^{-1}\mathbf{D}_{r\theta}\mathbf{N}_S r dr, \quad \mathbf{K}_{rz}^S = \int_{r_1}^{r_2}\mathbf{B}_S^T\mathbf{D}_{rz}\mathbf{N}_S r dr, \\
&\mathbf{K}_{ro}^S = \int_{r_1}^{r_2}\mathbf{B}_S^T r^{-1}\mathbf{D}_{ro}\mathbf{N}_S r dr, \quad \mathbf{K}_{\theta\theta}^S = \int_{r_1}^{r_2}\mathbf{N}_S^T r^{-2}\mathbf{D}_{\theta\theta}\mathbf{N}_S r dr, \quad \mathbf{K}_{\theta z}^S = \int_{r_1}^{r_2}\mathbf{N}_S^T r^{-1}\mathbf{D}_{\theta z}\mathbf{N}_S r dr, \\
&\mathbf{K}_{\theta o}^S = \int_{r_1}^{r_2}\mathbf{N}_S^T r^{-2}\mathbf{D}_{\theta o}\mathbf{N}_S r dr, \quad \mathbf{K}_{zz}^S = \int_{r_1}^{r_2}\mathbf{N}_S^T\mathbf{D}_{zz}\mathbf{N}_S r dr, \quad \mathbf{K}_{zo}^S = \int_{r_1}^{r_2}\mathbf{N}_S^T r^{-1}\mathbf{D}_{zo}\mathbf{N}_S r dr, \\
&\mathbf{K}_{oo}^S = \int_{r_1}^{r_2}\mathbf{N}_S^T r^{-2}\mathbf{D}_{oo}\mathbf{N}_S r dr, \quad \mathbf{M}^S = \int_{r_1}^{r_2}\mathbf{N}_S^T\rho_S\mathbf{N}_S r dr, \quad \mathbf{K}_{rr}^F = \int_{r_2}^{r_3}\mathbf{B}_F^T\rho_F^{-1}\mathbf{B}_F r dr, \\
&\mathbf{K}_{\theta\theta}^F = \int_{r_2}^{r_3}\mathbf{N}_F^T\rho_F^{-1}r^{-2}\mathbf{N}_F r dr, \quad \mathbf{K}_{zz}^F = \int_{r_2}^{r_3}\mathbf{N}_F^T\rho_F^{-1}\mathbf{N}_F r dr, \quad \mathbf{M}^F = \int_{r_2}^{r_3}\mathbf{N}_F^T\rho_F^{-1}c_F^{-2}\mathbf{N}_F r dr, \\
&\mathbf{C}_{SF} = \int_{r_2}^{r_2}\mathbf{N}_S^T\mathbf{n}_f\mathbf{N}_F r dr,
\end{aligned}
\tag{B2}
$$

where, $\mathbf{B}_S = \bar{\mathbf{B}}_S\otimes\mathbf{I}_{3\times3}$, $\bar{\mathbf{B}}_S = [dN_S^1/dr,...,dN_S^{m_S}/dr]$ and $\mathbf{B}_F = [dN_F^1/dr,...,dN_F^{m_F}/dr]$. Also $\mathbf{n}_f = \{\pm1\ 0\ 0\}^T$ is the unit normal for the solid-fluid interface using the appropriate sign at each interface. By rearranging the degrees of freedom (r then θ and z), the quadratic eigenvalue problem in (A2) can be converted to the generalized eigenvalue problem in (5) with,

$$
\mathbf{K}_2^S = \begin{bmatrix} \tilde{\mathbf{K}}_{rr}^{S2} & \mathbf{0} & -\tilde{\mathbf{K}}_{rz}^{S1} \\ \mathbf{0} & \tilde{\mathbf{K}}_{\theta\theta}^{S2} & -\tilde{\mathbf{K}}_{\theta z}^{S1} \\ \mathbf{0} & \mathbf{0} & \tilde{\mathbf{K}}_{zz}^{S2} \end{bmatrix},\ \mathbf{K}_0^S = \begin{bmatrix} \tilde{\mathbf{K}}_{rr}^{S0} & \tilde{\mathbf{K}}_{r\theta}^{S0} & \mathbf{0} \\ \tilde{\mathbf{K}}_{\theta r}^{S0} & \tilde{\mathbf{K}}_{\theta\theta}^{S0} & \mathbf{0} \\ \tilde{\mathbf{K}}_{zr}^{S1} & \tilde{\mathbf{K}}_{z\theta}^{S1} & \tilde{\mathbf{K}}_{zz}^{S0} \end{bmatrix},
\tag{B3}
$$

and $\boldsymbol{\phi}_S = \{ik_z\tilde{\boldsymbol{\phi}}_{Sr}^T \quad ik_z\tilde{\boldsymbol{\phi}}_{S\theta}^T \quad \tilde{\boldsymbol{\phi}}_{Sz}^T\}^T$. Note that the fluid contribution matrices in (B2) are only defined for the exterior fluid half-space $(r_2\le r)$. The associated matrices and interaction terms have to be considered for the fluid inside the tube $(r\le r_1)$, if exists.